RESEARCH ARTICLE

Check for updates

LiVTeO₅: a mid-infrared nonlinear optical vanadium tellurate crystal exhibiting enhanced second harmonic generation activities and notable birefringence†

Yuheng She,[a] Jinmiao Jiao,[a] Zheng Wang,[b] Jing Chai,[a] Song Jie,[a] Ning Ye,[a] Zhanggui Hu,[a] Yicheng Wu[a] and Conggang Li [ID] *[a]

Mid-infrared (IR) nonlinear optical (NLO) crystals are of great interest for applications in laser science and technology. Nevertheless, the pursuit of mid-IR NLO crystals displaying exceptional comprehensive performance remains a challenge. Herein, an effective strategy is achieved by combining two distinct species of second-order Jahn–Teller distorted cations, Te^{4+} and V^{5+}, into one compound. A prospective NLO vanadium tellurate crystal, $LiVTeO_5$, was synthesized *via* spontaneous crystallization, which crystallizes in the orthorhombic space group $P2_12_12_1$ (no. 19) with a three-dimensional framework structure. The optical measurements revealed that $LiVTeO_5$ manifests a large band gap of 3.2 eV and an intense second-harmonic-generation (SHG) activity of 3.2 × KDP. Moreover, it displays an extensive transmittance region beyond 5.0 μm, along with a discernible birefringence of 0.091, thereby facilitating the realization of the phase matching conditions. Additionally, structural analysis combined with first-principles calculations elucidate that the $[TeO_3]$ and $[VO_5]$ active building blocks primarily contribute to the intriguing macroscopic nonlinearity and notable birefringence observed in $LiVTeO_5$. These findings highlight the optimized overall properties of $LiVTeO_5$, which makes it a potential mid-IR NLO material.

Introduction

Nonlinear optical (NLO) materials capable of generating coherent and tunable lasers through frequency conversion capability, particularly those with the mid-infrared (IR) region covering the crucial atmospheric window (3–5 μm), have garnered significant interest in science and technology.[1–5] In recent years, significant strides have been made in the realm of design, synthesis, property characterization, and structure–property elucidation of mid-IR NLO compounds. Prominent examples include commercially available chalcogenide- and pnictide-based crystals, $AgGaQ_2$ (Q = Se, S) and $ZnGeP_2$.[6–8] Nevertheless, the practical applications of these materials are hampered by inherent limitations, such as poor laser damage

[a]Tianjin Key Laboratory of Functional Crystal Materials, Institute of Functional Crystal, Tianjin University of Technology, Tianjin 300384, China.
E-mail: cgli@email.tjut.edu.cn
[b]School of Physics and Electronic Engineering, Xingtai University, Xingtai 054001, China

thresholds for $AgGaQ_2$ and pronounced two-photon absorption at the conventional wavelength of 1 μm for $ZnGeP_2$.[9] In contrast to chalcogenides and pnictides, oxides have emerged as extensively employed NLO materials in commercial applications, exemplified by KH_2PO_4 (KDP), β-BaB_2O_4 (β-BBO), LiB_3O_5 (LBO), $KTiOPO_4$ (KTP) and $LiNbO_3$ (LN),[10–15] attributed to their large band gaps and high laser damage thresholds. Regrettably, most oxide crystals are incapable of supporting the fabrication of NLO devices that operate beyond 5.0 μm.[16] Consequently, there exists an urgent imperative to target novel IR NLO oxide crystals that offer favorable overall performance.

To manifest a second-order NLO effect, the paramount precondition is that the compound must crystallize in a non-centrosymmetric (NCS) structural form. Previous findings have shown that incorporating transition metal-based cations, susceptible to the second-order Jahn–Teller (SOJT) effect, into the structure constitutes an effective strategy for inducing a desirable NCS configuration.[17–20] Among the SHG-active d⁰ cations, the average distortive magnitude roughly adheres to the following hierarchy: $Mo^{6+} \approx V^{5+} > W^{6+} > Ti^{4+} > Nb^{5+} > Ta^{5+} > Zr^{4+}$. This suggests that the introduction of V^{5+} cations can enhance the probability of achieving an amplified SHG response.[19] Furthermore, V atoms have versatile coordination modes, encompassing $[VO_4]$, $[VO_5]$, and $[VO_6]$ polyhedral arrange-

This journal is © the Partner Organisations 2023

Inorg. Chem. Front., 2023, **10**, 6557–6565 | **6557**

ments, thereby allowing for diverse structural configurations.[21] Apart from the d^0 cations, the introduction of stereo-chemically active lone pair (SCALP) cations, exemplified by heavy element ions like Te^{4+}, has garnered considerable interest owing to their capability to construct SHG-active chromophores and elicit a red-shift in the IR absorption cutoff. For instance, the NLO tellurate crystal Li_2ZrTeO_6, which replaces Nb in $LiNbO_3$ with Te and Zr, extends the IR transmission cutoff edge to 7.4 μm.[22–26]

Drawing upon these ideas, we propose that by incorporating both V^{5+} and Te^{4+} ions, both of which are susceptible to the SOJT effect, into one compound, a pronounced structural distortion and a wide infrared (IR) transmission range can be effectively maintained.[27] Consequently, the vanadium tellurate crystal $LiVTeO_5$ (LVTO), which possesses an acentric orthorhombic structure analyzed through powder X-ray diffraction in 1973,[28] has piqued our interest as it aligns with our analysis strategy. However, investigations regarding the NLO properties of LVTO have remained absent from the scientific discourse. Accordingly, we successfully fabricated a high-quality vanadium tellurate crystal, LVTO, through a spontaneous crystallization technique. By optimizing the structure constructed from the NLO-active functional units $[VO_5]$ and $[TeO_3]$, LVTO achieves a well-balanced optical performance. In this study, we report the preparation, crystal growth, structural analysis, thermal behavior, and optical characterization of LVTO by the combination of experimental and theoretical approaches.

Experimental

Polycrystalline synthesis

The polycrystalline LVTO was obtained utilizing a stoichiometric one-step solid-phase reaction technique. The starting materials including Li_2CO_3 (Alfa Aesar, 99.9%), V_2O_5 (Alfa Aesar, 99.9%) and TeO_2 (Aladdin, 99.9%) according to their stoichiometric ratio were manually ground in an agate mortar and preheated at 350 °C for 10 h in a muffle furnace, followed by calcination at 480 °C for 72 h with several intermediate regrinding rounds. Powder X-ray diffraction (PXRD) analysis was employed to examine the phase purity of the target product.

Powder X-ray diffraction (PXRD)

A Rigaku SmartLab 9 kW diffractometer equipped with a diffraction monochromator setting for Cu K_α radiation (λ = 1.5418 Å) was used to record the PXRD data of the target compound. The test was performed over the range $10° \leq 2\theta \leq 70°$ at a scan step width of 0.01° with a fixed counting time of 0.3 s.

Thermal property analysis

The thermal behavior was analyzed for the LVTO crystalline samples with a NETZSCH STA 449F5 TG/DTA thermal analyzer. LVTO polycrystalline specimens, weighing approximately 12.5 mg, were carefully introduced into an Al_2O_3 crucible. The

crucible was subjected to a controlled heating process, gradually raising the temperature from ambient conditions to 600 °C at a heating rate of 10 °C per minute under a flowing nitrogen gas atmosphere.

Energy-dispersive spectroscopy (EDS) analysis

To probe the elemental ratios in the LVTO crystal, elemental distribution maps and microprobe elemental analyses were recorded using a field-emission scanning electron microscope (FEI Quanta FEG 250).

Structural characterization

Single crystal data were collected through single crystal X-ray diffraction experiments on a Bruker D8 VENTURE CMOS X-ray source at a constant temperature with Mo Kα radiation (λ = 0.71073 Å). Cell refinement, data integration, and absorption correction were implemented using the APEX III software. The preliminary crystal structure data were resolved by direct methods using the SHELXTL crystallographic software package. Comprehensive structural parameter data are presented and elucidated in Tables S1–S3 (ESI†), which involve the atomic coordinates, equivalent isotropic displacement parameters, interatomic distances and angles, and the bond valence sums (BVS) for all atoms. The corresponding experimental conditions and the refined crystallographic data are available in Table 1.

UV-visible diffuse reflectance spectra

The ultraviolet-visible (UV-vis) diffuse reflectance spectra were gauged from 200 to 2000 nm utilizing a Hitachi UH4150 spectrophotometer at ambient temperature, while $BaSO_4$ was selected as the diffuse reflectance standard sample. The Kubelka–Munk remission function was employed to transform reflectance spectra into absorbance: $F(R) = (1 - R)^2/(2R) = K/S$, where R is the reflectance, K is the absorption and S is the scattering.[29]

Table 1 Crystallographic data and structural refinement of LVTO

Empirical formula	$LiVTeO_5$
Formula weight	265.48
Temperature (K)	298(2)
Wavelength (Å)	0.71073
Crystal system	Orthorhombic
Space group	$P2_12_12_1$
a (Å)	5.2789(2)
b (Å)	8.3415(2)
c (Å)	9.5082(3)
Volume (Å³)	418.68(2)
Z	4
Density (g cm⁻³)	4.212
F (000)	472
R (int)	0.0451
Completeness	100%
GOF on (F^2)	1.079
Final R indices $[F_o^2 > 2\sigma(F_o^2)]^a$	$R_1 = 0.0133$, w$R_2 = 0.0341$
R indices (all data)	$R_1 = 0.0139$, w$R_2 = 0.0344$
CCDC number	2289244

$^a R_1 = \sum||F_o| - |F_c||/\sum|F_o|$; w$R_2 = [\sum w(F_o^2 - F_c^2)^2/\sum w(F_o^2)^2]^{1/2}$.

IR spectroscopy and Raman spectra

The IR spectra of the LVTO powder samples were characterized using a Nicolet iS50 FT-IR infrared spectrometer at ambient temperature across a spectral range of 400–4000 cm^{-1}. About 3.5 mg samples were placed on the test platform for testing. Raman spectroscopy measurements were recorded on a WITECalpha300R spectrometer equipped with a CCD detector using 532 nm excitation radiation at ambient temperature. The measurements were performed in the range of 100 to 1100 cm^{-1}.

Second-harmonic-generation tests

Second harmonic generation (SHG) tests were performed on the polycrystalline samples of LVTO using a Q-switched Nd: YAG laser with a fundamental wavelength of 1064 nm, following the Kurtz–Perry method. A powdered microcrystalline sample of LVTO was thoroughly ground and then sieved into several distinct particle size ranges of 50–75, 75–109, 109–120, 120–150, 150–180, and 180–212 μm. For comparison of SHG activities, KH_2PO_4 (KDP) with the same particle size ranges were also prepared as the measured reference patterns.

Birefringence characterization

The optical birefringence of the target compound was experimentally examined through a polarizing microscope (Nikon Eclipse E200MV POL) with a visible light source. The corresponding birefringence value can be collected following the equation: $R = \Delta n \times D = |N_e - N_o| \times D$, where Δn denotes the birefringence, D refers to the crystal thickness, R signifies the retardation, and N_e and N_o represent the birefringence of the extraordinary wave and the ordinary wave, respectively.[30] A pristine crystal was chosen and its thickness was ascertained employing a Bruker SMART APEX III CCD diffractometer.

Computational details

We performed first-principles calculations using density functional theory (DFT) calculations within the Cambridge sequential total energy package (CASTEP) software to analyze the electronic density difference and band structure of the LVTO crystal.[31] In order to accurately comprehend the microcosmic mechanism of the LVTO crystal, the exchange–correlation effects were described using the Perdew–Burke–Ernzerhof (PBE) functional with the generalized gradient approximation (GGA) scheme.[32–34] Norm-conserving pseudopotentials were utilized with the following valence electron configuration: Li $2s^1$, Te $5s^25p^4$, V $3d^34s^2$, and O $2s^22p^4$. To ensure reliable simulation results, the plane-wave cutoff energy was set to 810 eV, and a Monkhorst–Pack scheme k-point mesh of $6 \times 4 \times 4$ in the first Brillouin zone was used for sampling and numerical integration.

Results and discussion

Powder X-ray diffraction (PXRD) and thermal analysis

Polycrystalline samples of LVTO were synthesized employing solid-state methodologies. The phase purity of LVTO was authenticated through PXRD Rietveld refinement, utilizing the Toolbar FullProf Suite program. As shown in Fig. 1a, the PXRD patterns of the as-synthesized samples match well with the calculated observations derived from the structural data. Additionally, the thermal durability of LVTO was assessed *via* precise measurements of DSC and TGA. Fig. 1b demonstrates that the DSC curves exhibit one appreciable endothermic peak at approximately 498 °C upon heating, while the TG curves demonstrate no weight loss over the test temperature range. These results suggest that LVTO possesses good thermal stability without undergoing any phase transition. Moreover, the powder PXRD patterns of the melted solid agree well with
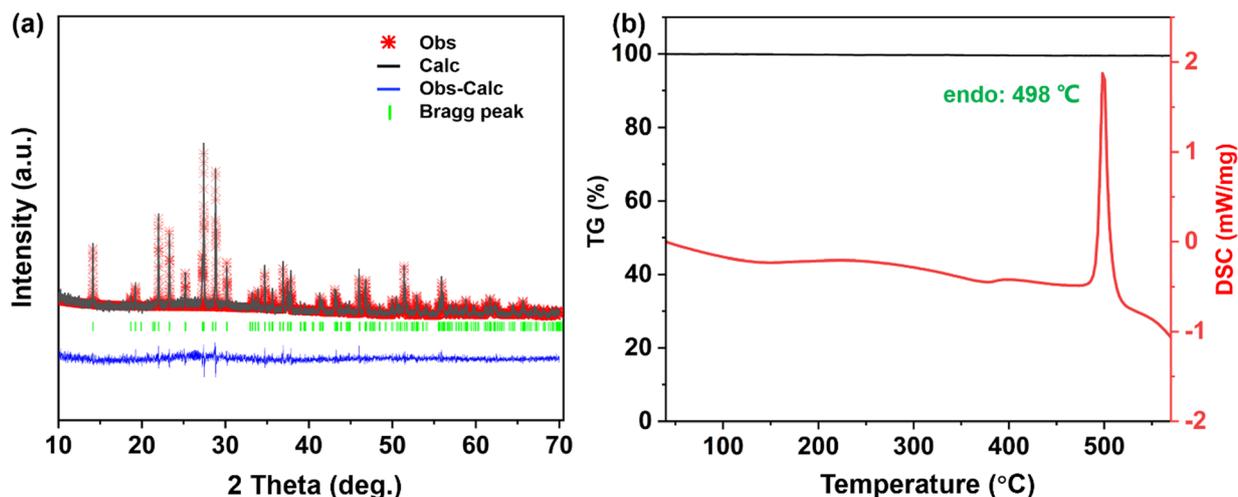

Fig. 1 (a) Rietveld refinement patterns: calculated data (black line), experimental data (red asterisk), and the difference (blue trace) between them. The tick marks (green) display the expected Bragg reflections. (b) DSC and TG curves for LVTO.

This journal is © the Partner Organisations 2023

Inorg. Chem. Front., 2023, **10**, 6557–6565 | **6559**

those of the initial LVTO, revealing that LVTO is a congruent compound (Fig. S1†).

Crystal growth and the structure of LVTO

LVTO crystals were prepared using an optimized spontaneous nucleation technique. After conducting several rounds of experiments, we successfully cultivated bulk single crystals of LVTO with dimensions of $2 \times 2 \times 1.5$ mm^3, as exemplified in Fig. S2.† The structural information of LVTO was first determined through powder X-ray diffraction in 1973.[28] To delve deeper into the intricate interplay between the structure and properties, single-crystal XRD was then employed to reconfirm the structure of LVTO. The title compound crystallized in an acentric orthorhombic configuration with the space group $P2_12_12_1$ (no. 19). The refined unit cell parameters were discerned to be $a = 5.2789(2)$ Å, $b = 8.3415$ (2) Å, $c = 9.5082$ (3) Å, and $\beta = 90°$. One independent Li atom, one independent Te atom, one independent V atom, and five O atoms were observed in the asymmetric unit of LVTO. As shown in Fig. 2a, the V atom is surrounded by five O atoms, forming a distorted trigonal bipyramidal geometry [VO_5] with V–O lengths ranging from 1.642(3) to 2.055(3) Å. The Te^{4+} cation adopts a triangular out-of-plane coordination with three O atoms, and the lengths of the three Te–O bonds are in the range of 1.852(3) to 1.912(3) Å due to the presence of Te^{4+} lone pair electrons. Each [TeO_3] triangular pyramid intertwines with three neighboring [VO_5]

square pyramids *via* shared oxygen atoms, orchestrating the construction of [TeV_3O_{15}]$^{11-}$ zigzag grids (Fig. 2b). These [TeV_3O_{15}]$^{11-}$ zigzag grids are further interconnected to form a three-dimensional (3D) framework structure, in which all Li$^+$ cations are bonded in a 5-coordinate geometry (Fig. S3†) and are located in the cavities to balance the charge (Fig. 2c). Notably, this remarkable 3D framework unveils a quintessential honeycomb-like configuration, with tunnels that stretch indefinitely along the a axis as presented in Fig. 2d.

In terms of the formula, LiVTeO$_5$ and LiNbTeO$_5$ can be considered as LiATeO$_5$ (A = V, Nb).[24] However, by substituting V^{5+} cations in LTVO with Nb^{5+} cations of the same main group in the NLO crystal LiNbTeO$_5$, it crystallizes in the $P2_1$ space group, which is non-isotypic to LVTO. To further elucidate this situation, a comparative analysis of their structural features was conducted. In LVTO, V^{5+} cations are all five-coordinated and adopt a distorted trigonal bipyramidal geometry, while the Nb^{5+} cations in LiNbTeO$_5$ are located in a distorted octahedral environment. Additionally, one [TeO_3] triangular pyramid and three adjacent [NbO_6] octahedra in LiNbTeO$_5$ are linked by corner sharing to form [$TeNb_3O_{17}$]$^{15-}$ and [$TeNb_3O_{18}$]$^{17-}$ zigzag grids, respectively (Fig. 2e). As shown in Fig. 2f and g, the 3D structure of LiNbTeO$_5$ also displays characteristics of honeycomb-like channels similar to those in LVTO. Furthermore, unlike the independent [VO_5] polyhedra in LVTO, the [NbO_6] octahedra are interconnected to form [Nb_2O_{10}]$_\infty$ zigzag chains

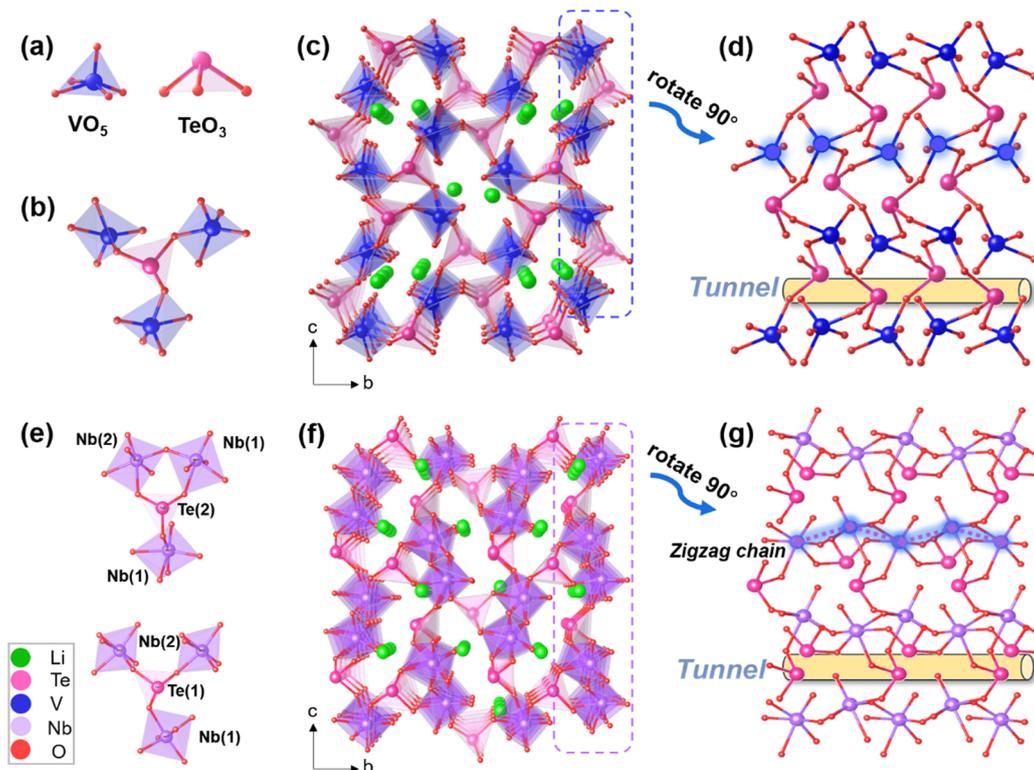**Fig. 2** Structural characterization. (a) [VO_5] and [TeO_3] motifs. (b) The [TeV_3O_{15}]$^{11-}$ fundamental building block of LVTO. (c) 3D honeycomb-like framework of LVTO. (d) The crystal structure of LVTO viewed along the *ac* plane. (e) The [$TeNb_3O_{17}$]$^{15-}$ and [$TeNb_3O_{18}$]$^{17-}$ building blocks of LiNbTeO$_5$. (f) 3D honeycomb-like framework of LiNbTeO$_5$. (g) The crystal structure of LiNbTeO$_5$ viewed along the *ac* plane.

6560 | *Inorg. Chem. Front.*, 2023, **10**, 6557–6565

This journal is © the Partner Organisations 2023

in LiNbTeO$_5$. It is suspected that the disparate evolutionary trajectories of these structures give rise to variations in their symmetrical attributes.

In addition, bond valence sum (BVS) calculations reveal the expected oxidation states of 3.80, 5.09 and 2.03 for Te, V and O, respectively, which are consistent with those derived from the structural data of LVTO. Energy-dispersive spectroscopy (EDS) measurements corroborated the existence of V/Te/O with an average atomic ratio in a reasonable range for LVTO (Fig. S4†), which aligns well with the observations from the structural analysis.

Optical performance

The UV-vis diffuse reflectance spectrum of the polycrystalline LVTO revealed that the UV cut-off edge occurs at approximately 357 nm, corresponding to an experimental band gap of 3.2 eV (Fig. 3a), as determined utilizing the Kubelka–Munk formula equation. Moreover, the IR spectroscopy of LVTO is presented in Fig. 3b, demonstrating its high mid-IR transparency up to

914 cm^{-1}, which covers a critical atmospheric transparent window (3–5 μm). Additionally, the absorption peak characteristics associated with V–O and Te–O vibrations in the IR spectrum were analyzed. The bands located at 796, 865, and 914 cm^{-1} predominantly originate from the V–O vibration. The bands at around 600–740 cm^{-1} are mainly attributed to the Te–O vibration. These peak assignments are consistent with those reported in previous studies.[35,36]

Furthermore, Raman spectrum tests were recorded to comprehensively identify vibration modes in structural analysis. As shown in Fig. S5,† the absorption bands located at 365, 645, and 737 cm^{-1} can be assigned to the characteristic symmetric and asymmetric stretching vibrations, as well as the bending vibration of [TeO$_3$], according to previous findings. The bands at around 750 cm^{-1} are attributed to the symmetric stretching vibration of [TeO$_3$] units. The Raman frequency-shifted peaks observed in the range of 790–920 cm^{-1} are mainly induced by the V–O stretching vibration. The bands ranging from 400 to 495 cm^{-1} are dominated by the Li–O vibrations. These above observations confirm
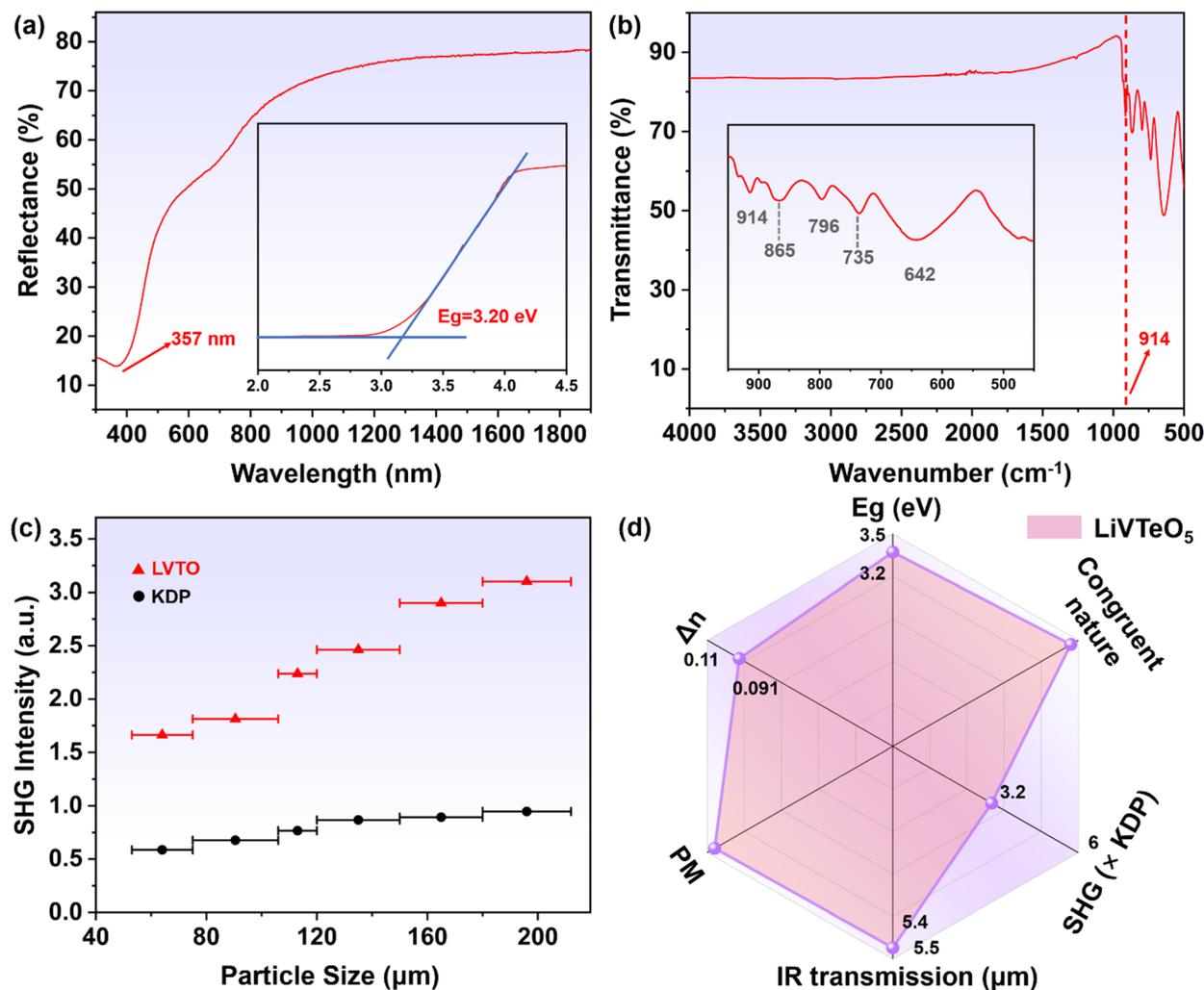
Fig. 3 Optical characterization of LVTO. (a) UV-vis diffuse-reflectance spectrum and the band gap. (b) IR transmission spectra. (c) Phase-matching curves for LVTO and KDP, respectively. (d) The overall NLO performance of LVTO.

This journal is © the Partner Organisations 2023

Inorg. Chem. Front., 2023, **10**, 6557–6565 | **6561**

the presence of $[TeO_3]$ and $[VO_5]$ groups, which corresponds well to the single crystal structure of LVTO.[23,35,37]

SHG measurement

As the LVTO compound crystallizes in the $P2_12_12_1$ space group and lacks an inversion center within the crystal structure, the Kurtz–Perry method was employed to evaluate its powder SHG performance under a Q-switched Nd:YAG laser (1064 nm).[38] As depicted in Fig. 3c, the SHG signals of LVTO exhibit enhancement with increasing particle size, and eventually reaching saturation, which implies that LVTO follows the phase-matchable rule. Within the particle size range of 180–212 μm, it is noteworthy that the LVTO compound exhibits a pronounced SHG intensity of 3.2 times that of KDP. Moreover, the desirable SHG activities of LVTO are comparable to those of other NLO tellurates, such as $Li_2ZrTe_2O_6$ (2.5 × KDP) and Li_2SnTeO_6 (2.5 × KDP).[26,39] Hence, it is evident that the title compound exhibits commendable attributes (Fig. 3d), including a large band gap, a broad transmission window, and favorable SHG effects, making it a promising mid-IR NLO crystal.

Birefringence characterization

In order to achieve coherent light output, birefringence is a critical parameter for satisfying phase-matching conditions. The experimental birefringence of LVTO was quantified employing a cross-polarizing prism methodology. The precise thickness of the crystal plane was determined to be 11.7 μm utilizing a Bruker single crystal diffractometer, as depicted in Fig. 4a. When incident light passes through an anisotropic single crystal, it undergoes a division into two polarized beams. The refractive indices of the two polarized lights are not equal and the propagation speeds are distinct (N_o and N_e). The original interference color and the complete extinction of LVTO under orthogonally polarized light were confirmed to be second-order orange according to the Michel-Levy color chart in the inset of

Fig. 4b, and it achieves complete extinction through the employment of a Berek compensator. In accordance with the equation $R = \Delta n \times D$, the experimental measurement yielded a noteworthy value of 0.091 at the visible wavelength, suggesting that the birefringence is sufficiently substantial to facilitate phase matching. Moreover, the wavelength-dependent refractive indices for LVTO were also calculated, and the theoretical value of the birefringence was found to be 0.090 at 1064 nm as presented in Fig. 4b, in parallel with the experimental one. This value is also comparable to that of the commercial NLO and birefringent crystal $LiNbO_3$ (0.0786).[40,41]

Structure–property relationship

To elucidate the underlying relationship between the structural characteristics and optical properties, theoretical calculation was carried out for LVTO.[42] As shown in Fig. 5a, the band structures indicate that LVTO belongs to an indirect band gap compound with a theoretical band gap value of 2.60 eV, which is consistent with the experimental observation. Fig. 5b illustrates the detailed total and partial density of states (PDOS), revealing that the near-forbidden-gap states are mainly contributed by Te, V and O atoms, while the contribution of the Li atom is relatively limited. Specifically, the electron states near the bottom of the conduction bands (CB) ranging from 2.0 to 7.0 eV are predominantly dominated by the 5p orbitals of tellurium and the 3d orbitals of vanadium, with the 2s orbitals of lithium making a smaller contribution. The behavior of Li orbitals can be ascribed to their coordination in a five-coordinated $[LiO_5]$ environment, which induces a structural distortion. The band positions in proximity to the maximum of the valence band (VB) spanning from −5.0 to 0.0 eV predominantly derive from oxygen 2p orbitals, showcasing extensive hybridization with tellurium 5p and vanadium 3d orbitals. The electron states in the range of −7 to −10 eV are mainly composed of the hybridizations of Te 5s and O 2p states.
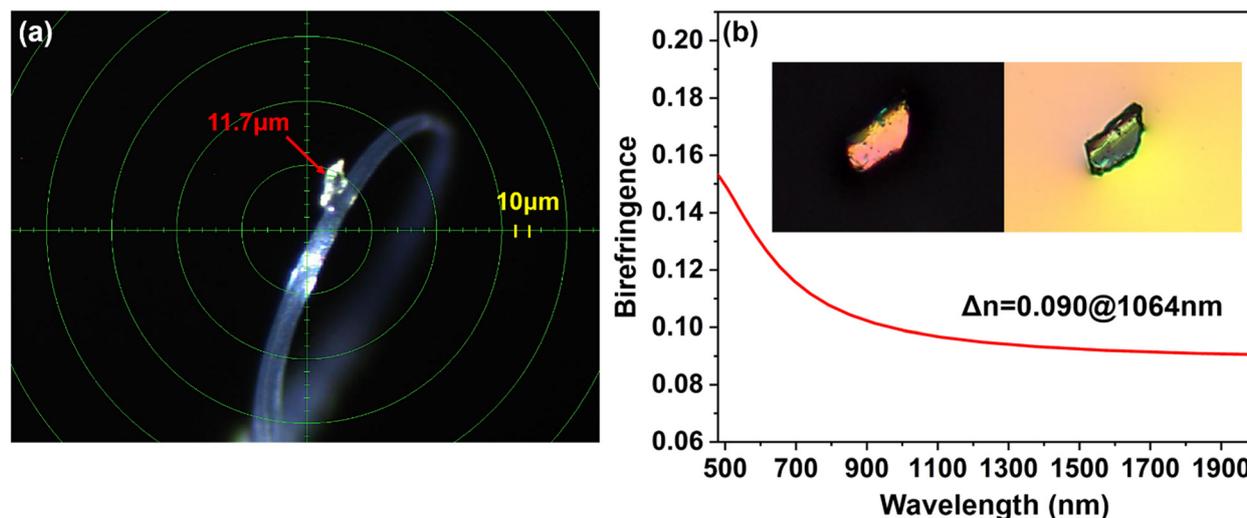

Fig. 4 Birefringence measurements for LVTO. (a) The measured thickness of the LVTO crystal. (b) The theoretical refractive index dispersion curves with the insets representing the original interference color and the complete extinction state of LVTO.
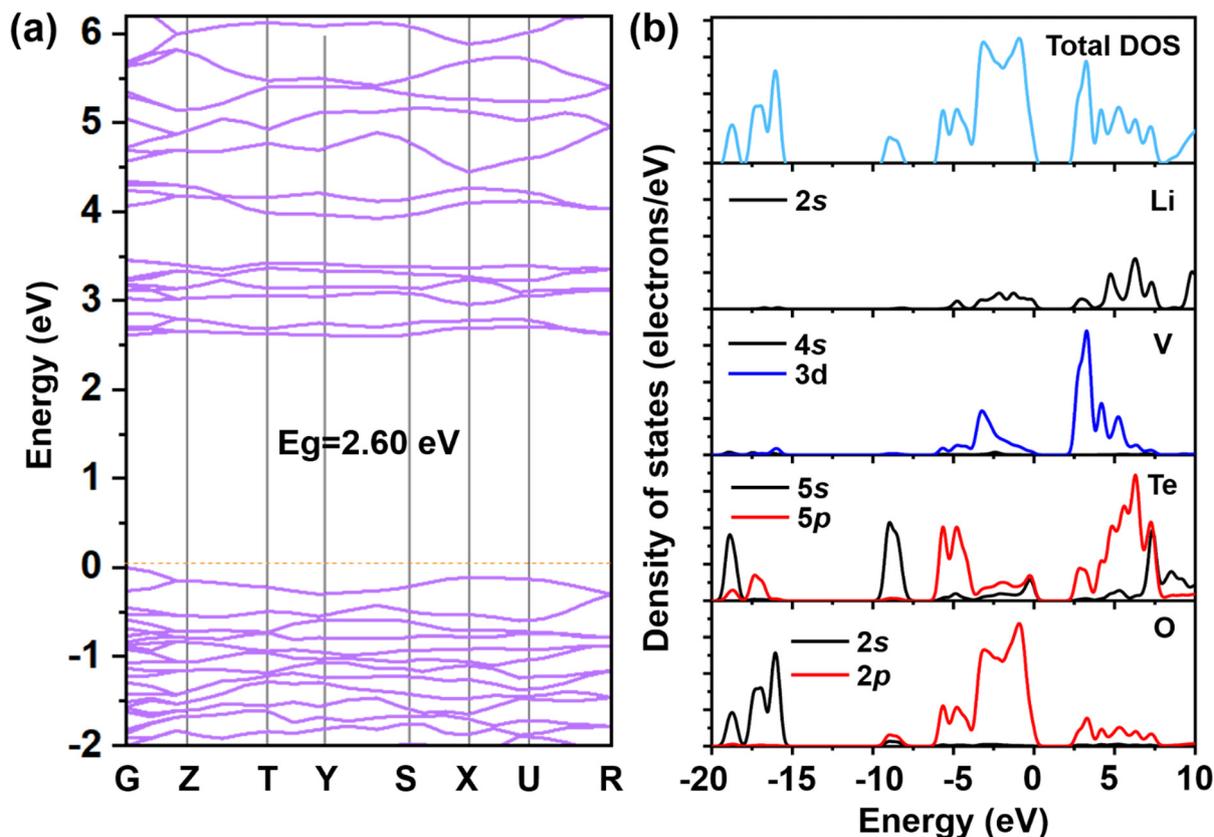
6562 | *Inorg. Chem. Front.*, 2023, **10**, 6557–6565

This journal is © the Partner Organisations 2023

Fig. 5 Calculated electronic structure of LVTO. (a) Energy band structure. (b) Total DOS and partial DOS.

Based on these analyses, it can be perceived that the SOJT distortive building motifs $[TeO_3]$ and $[VO_5]$ are mainly responsible for the appreciable NLO activity of LVTO.

To further quantitatively elucidate the contribution of these groups to NLO performance, the local dipole moments of structural motifs in LVTO were examined utilizing the bond-valence approach methodology. As illustrated in Fig. S6,† the orientations of the dipole moments for these groups within one unit cell exhibit inconsistency, which is distinct from those observed in $LiNbTeO_5$. The magnitudes of the dipole moments for the individual $[TeO_3]$, $[VO_5]$ and $[LiO_5]$ polyhedra were calculated and found to be 21.98, 4.42 and 2.87 Debye, respectively (Table S4†).

Conclusions

In summary, a prospective NLO vanadium tellurate crystal, $LiVTeO_5$, was designed by combining SOJT distorted cations Te^{4+}, with stereochemically-active lone pairs, and V^{5+} cations characterized by a d^0 electronic configuration. Optical characterization demonstrated that the aforementioned compound achieves a favorable balance of crucial optical properties, including an amplified SHG response of $3.2 \times$ KDP, a large band gap of (3.2 eV), an extensive transmittance region, and a sufficient birefringence of 0.091 at the visible wavelength, enabling phase match-

ing capability. First-principles calculations implied that the NLO and birefringent performance can be intuitively ascribed to the highly distortive units $[TeO_3]$ and $[VO_5]$. Our findings unveil the promising potential of $LiVTeO_5$ in NLO applications and pave the way for the exploration of novel mid-IR NLO materials exhibiting desirable performance.

Conflicts of interest

The authors declare no competing financial interest.

Acknowledgements

References

1 X. Jiang, S. Deng, M. H. Whangbo and G. Guo, Material research from the viewpoint of functional motifs, *Natl. Sci. Rev.*, 2022, **9**, nwac017.

This journal is © the Partner Organisations 2023

Inorg. Chem. Front., 2023, **10**, 6557–6565 | **6563**

2 G. Han, Y. Wang, X. Su, Z. Yang and S. Pan, Growth, properties, and theoretical analysis of M_2LiVO_4 (M = Rb, Cs) crystals: two potential Mid-Infrared nonlinear optical materials, *Sci. Rep.*, 2017, **7**, 1901.

3 C. Wu, X. Jiang, L. Lin, Y. Hu, T. Wu, Z. Lin, Z. Huang, M. G. Humphrey and C. Zhang, A congruent-melting mid-infrared nonlinear optical vanadate exhibiting strong Second-Harmonic Generation, *Angew. Chem., Int. Ed.*, 2021, **60**, 22447–22453.

4 H. Lan, F. Liang, X. Jiang, C. Zhang, H. Yu, Z. Lin, H. Zhang, J. Wang and Y. Wu, Pushing nonlinear optical oxides into the mid-infrared spectral region beyond 10 µm: Design, synthesis, and characterization of $La_3SnGa_5O_{14}$, *J. Am. Chem. Soc.*, 2018, **140**, 4684–4690.

5 J. Jiao, F. Liang, C. Li, T. Han, W. Zhao, Y. She, N. Ye, Z. Hu and Y. Wu, Shedding light on the structure and characterization of $K_2ZnGe_2O_6$: A phase-matchable nonlinear optical crystal, *Inorg. Chem.*, 2022, **61**, 11471–11477.

6 B. Tell and H. M. Kasper, Optical and electrical properties of $AgGaS_2$ and $AgGaSe_2$, *Phys. Rev. B: Solid State*, 1971, **4**, 4455–4459.

7 U. Simon, Z. Benko, M. W. Sigrist, R. F. Curl and F. K. Tittel, Design considerations of an infrared spectrometer based on difference-frequency generation in $AgGaSe_2$, *Appl. Opt.*, 1993, **32**, 6650–6655.

8 G. D. Boyd, E. Buehler and F. G. Storz, Linear and nonlinear optical properties of $ZnGeP_2$ and CdSe, *Appl. Phys. Lett.*, 1971, **18**, 301–304.

9 F. Liang, L. Kang, Z. Lin and Y. Wu, Mid-Infrared nonlinear Optical materials based on metal chalcogenides: structure–property relationship, *Cryst. Growth Des.*, 2017, **17**, 2254–2289.

10 J. J. De Yoreo, A. K. Burnham and P. K. Whitman, Developing KH_2PO_4 and KD_2PO_4 crystals for the world's most power laser, *Int. Mater. Rev.*, 2013, **47**, 113–152.

11 C. Chen, B. Wu, A. Jiang and G. You, A new-type ultraviolet SHG crystal β-BaB_2O_4, *Sci. Sin., Ser. B*, 1985, **28**, 235–243.

12 C. Chen, Y. Wu, A. Jiang, B. Wu, G. You, R. Li and S. Lin, New nonlinear-optical crystal: LiB_3O_5, *J. Opt. Soc. Am. B*, 1989, **6**, 616.

13 V. G. Dmitriev, G. G. Gurzadyan, D. N. Nikogosyan and C. Braun, Handbook of nonlinear optical crystals, *Appl. Opt.*, 1999, **31**, 3225–3231.

14 G. D. Boyd, R. C. Miller, K. Nassau, W. L. Bond and A. Savage, $LiNbO_3$: an efficient phase matchable nonlinear optical material, *Appl. Phys. Lett.*, 1964, **5**, 234–236.

15 C. Wu, G. Yang, M. G. Humphrey and C. Zhang, Recent advances in ultraviolet and deep-ultraviolet second-order nonlinear optical crystals, *Coord. Chem. Rev.*, 2018, **375**, 459–488.

16 Q. Wu, J. Zhou, X. Liu, X. Jiang, Q. Zhang, Z. Lin and M. Xia, $Ca_3(TeO_3)_2(MO_4)$ (M = Mo, W): Mid-Infrared nonlinear optical tellurates with ultrawide transparency ranges and superhigh Laser-Induced Damage Thresholds, *Inorg. Chem.*, 2021, **60**, 18512–18520.

17 W. Zhao, C. Li, T. Han, J. Jiao, Y. She, D. Ju, F. Liang, N. Ye, Z. Hu and Y. Wu, $Cs_2Bi_2OSi_2O_7$: A promising bismuth silicate nonlinear optical crystal with face-sharing BiO_5 polyhedra exhibiting strengthened Second Harmonic Generation response and birefringence, *Chem. Mater.*, 2022, **34**, 3365–3372.

18 M. Xia, X. Jiang, Z. Lin and R. Li, "All-Three-in-One": A new bismuth–tellurium–borate Bi_3TeBO_9 exhibiting strong Second Harmonic Generation response, *J. Am. Chem. Soc.*, 2016, **138**, 14190–14193.

19 K. M. Ok, P. S. Halasyamani, D. Casanova, M. Llunell, P. Alemany and S. Alvarez, Distortions in octahedrally coordinated d^0 transition metal oxides: A continuous symmetry measures approach, *Chem. Mater.*, 2006, **18**, 3176–3183.

20 X. Guo, Z. Gao and X. Tao, Recent advances in tellurite molybdate/tungstate crystals, *CrystEngComm*, 2022, **24**, 7516–7529.

21 Y. Kikukawa, K. Seto, S. Uchida, S. Kuwajima and Y. Hayashi, Solid-state umbrella-type inversion of a VO_5 square-pyramidal unit in a Bowl-type dodecavanadate induced by insertion and elimination of a guest molecule, *Angew. Chem., Int. Ed.*, 2018, **57**, 16051–16055.

22 Q. Wang, X. Dong, L. Huang, K. M. Ok, Z. Lin and G. Zou, $Cd_2Nb_2Te_4O_{15}$: A Novel Pseudo-Aurivillius-Type tellurite with unprecedented nonlinear optical properties and excellent stability, *Small*, 2023, **19**, 2302797.

23 Y. She, F. Liang, J. Jiao, W. Zhao, N. Ye, Z. Hu, Y. Wu and C. Li, A new stable polymorph of $Li_2TeMo_3O_{12}$ with wide mid-infrared transparency and a large Raman response, *Inorg. Chem. Front.*, 2023, **10**, 3595–3604.

24 K. Chen, C. Lin, G. Peng, Y. Chen, H. Huang, E. Chen, Y. Min, T. Yan, M. Luo and N. Ye, $LiNbTeO_5$: A high-performance multifunctional crystal material with a very large Second-Harmonic Generation response and piezoelectric coefficient, *Chem. Mater.*, 2021, **34**, 399–404.

25 M. Yan, H. Xue and S. Guo, Recent achievements in lone-pair cation-based infrared second-order nonlinear optical materials, *Cryst. Growth Des.*, 2020, **21**, 698–720.

26 (a) G. Zou and K. M. Ok, Novel ultraviolet (UV) nonlinear optical (NLO) materials discovered by chemical substitution-oriented design, *Chem. Sci.*, 2020, **11**, 5404–5409; (b) W. Lu, Z. Gao, X. Liu, X. Tian, Q. Wu, C. Li, Y. Sun, Y. Liu and X. Tao, Rational design of a $LiNbO_3$-like nonlinear optical crystal, Li_2ZrTeO_6, with high Laser-Damage Threshold and wide Mid-IR transparency window, *J. Am. Chem. Soc.*, 2018, **140**, 13089–13096.

27 J. Chen, C. Hu, F. Kong and J. G. Mao, High-performance Second-Harmonic-Generation (SHG) materials: new developments and new strategies, *Acc. Chem. Res.*, 2021, **54**, 2775–2783.

28 J. Darriet, Structure cristalline de la phase $LiVTeO_5$, *Bull. Mineral.*, 1973, **96**, 97–99.

29 P. Kubelka and F. Z. Munk, Ein Beitrag zur Optik der Farbanstriche (Contribution to the optic of paint), *Z. Tech. Phys.*, 1931, **12**, 593.

6564 | *Inorg. Chem. Front.*, 2023, **10**, 6557–6565

This journal is © the Partner Organisations 2023

30 W. Zhao, J. Jiao, Y. She, F. Liang, N. Ye, Z. Hu, Y. Wu and C. Li, Tailored ordered structures with functional units of distorted [NbO$_6$] and antiparallel [GeO$_4$] for enhanced birefringence in germanate crystal, *Adv. Opt. Mater.*, 2022, **10**, 2201704.

31 S. J. Clark, M. D. Segall, C. J. Pickard, P. J. Hasnip, M. J. Probert, K. Refson and M. C. Payne, First principles methods using CASTEP, *Z. Kristallogr.*, 2005, **220**, 567–570.

32 W. Kohn, Nobel Lecture: Electronic structure of matter—wave functions and density functionals, *Rev. Mod. Phys.*, 1999, **71**, 1253–1266.

33 V. Milman, K. Refson, S. J. Clark, C. J. Pickard, J. R. Yates, S. P. Gao, P. J. Hasnip, M. I. J. Probert, A. Perlov and M. D. Segall, Electron and vibrational spectroscopies using DFT, plane waves and pseudopotentials: CASTEP implementation, *J. Mol. Struct.: THEOCHEM*, 2010, **954**, 22–35.

34 A. M. Rappe, K. M. Rabe, E. Kaxiras and J. D. Joannopoulos, Optimized pseudopotentials, *Phys. Rev. B: Condens. Matter*, 1990, **41**, 1227–1230.

35 T. Sivakumar, K. M. Ok and P. S. Halasyamani, Synthesis, structure, and characterization of novel two- and three-dimensional vanadates: Ba$_{2.5}$(VO$_2$)$_3$(SeO$_3$)$_4$·H$_2$O and La(VO$_2$)$_3$(TeO$_6$)·3H$_2$O, *Inorg. Chem.*, 2006, **45**, 3602–3605.

36 D. W. Lee, S. J. Oh, P. S. Halasyamani and K. M. Ok, New quaternary tellurite and selenite: synthesis, structure, and characterization of centrosymmetric InVTe$_2$O$_8$ and noncentrosymmetric InVSe$_2$O$_8$, *Inorg. Chem.*, 2011, **50**, 4473–4480.

37 X. Li, Y. J. Wei, H. Ehrenberg, D. L. Liu, S. Y. Zhan, C. Z. Wang and G. Chen, X-ray diffraction and Raman scattering studies of Li$^+$/e$^-$-extracted inverse spinel LiNiVO$_4$, *J. Alloys Compd.*, 2009, **471**, L26–L28.

38 S. K. Kurtz and T. T. Perry, A powder technique for the evaluation of nonlinear optical materials, *J. Appl. Phys.*, 1968, **39**, 3798–3813.

39 X. Du, X. Guo, Z. Gao, F. Liu, F. Guo, S. Wang, H. Wang, Y. Sun and X. Tao, Li$_2$MTeO$_6$ (M=Ti, Sn): Mid-Infrared nonlinear optical crystal with strong Second Harmonic Generation response and wide transparency range, *Angew. Chem., Int. Ed.*, 2021, **60**, 23320–23326.

40 A. Tudi, S. Han, Z. Yang and S. Pan, Potential optical functional crystals with large birefringence: recent advances and future prospects, *Coord. Chem. Rev.*, 2022, **459**, 214380.

41 D. E. Zelmon, D. L. Small and D. Jundt, Infrared corrected Sellmeier coefficients for congruently grown lithium niobate and 5 mol% magnesium oxide –doped lithium niobate, *J. Opt. Soc. Am. B*, 1997, **14**, 3319.

42 T. Han, C. Li, W. Zhao, Y. She, J. Jiao, F. Liang, Z. Hu and Y. Wu, Investigations on the synthesis, crystal structure, linear- and nonlinear- optical properties of the zinc germanate Rb$_2$ZnGe$_2$O$_6$, *Inorg. Chem.*, 2022, **61**, 706–712.